# Shock-Buffet Prediction Report in Support of the High-Angle Working Group at the Third Aeroelastic Prediction Workshop

Pawel Chwalowski*, Garrett R. McHugh[†], and Steven J. Massey[‡]
*NASA Langley Research Center, Hampton, VA, 23681*

Lior Poplingher[§] and Daniella E. Raveh[¶]
*Technion-Israel Institute of Technology, Haifa, 3200003, Israel*

Adam Jirasek[‖] and Jurgen Seidel[**]
*High Performance Computing Research Center, USAFA*

Nicholas F. Giannelis[††] and Gareth A. Vio[‡‡]
*The University of Newcastle and The University of Sydney*

Kartik Venkatraman[§§] and Magan Singh[¶¶]
*Indian Institute of Science*

Behzad R. Ahrabi[***], Moeljo Hong[†††], and Jeffrey Slotnick[‡‡‡]
*The Boeing Company*

This paper presents a summary of the computational shock-buffet results associated with the third Aeroelastic Prediction Workshop (AePW-3) High-Angle Working Group. The computational results are compared against experimental data collected during the Oscillating Turn Table (OTT) Benchmark Supercritical Wing (BSCW) test campaign conducted in NASA Langley Research Center Transonic Dynamics Tunnel (TDT) in early 2000. In addition to experimental forced oscillation data, unsteady pressure data was collected at a single spanwise station at transonic Mach numbers, several values of dynamic pressure, and fixed angles of attack. It is acknowledged that the current experimental data are limited, but future experiments are planned to obtain pressure data at two wingspan stations in addition to unsteady Pressure Sensitive Paint (uPSP). With that, the computational results presented here are considered to be semi-blind. The results are presented in the form of time-varying pressure coefficients, running-mean values of the pressure coefficients, Power Spectral Density (PSD) and Strouhal number computations. The results are split into two parts. In the first part, the computational results obtained by each team using their flow solvers and grids are compared. In the second part, a single computational tool was used to compute unsteady pressure on participant-generated grids. In addition, a description of each participating team's software and methods is included.

---

*Research Engineer

[†]Research Engineer, AIAA Member.

[‡]Research Engineer, AIAA Senior Member.

[§]Graduate Student, Faculty of Aerospace Engineering.

[¶]Professor, Faculty of Aerospace Engineering, AIAA Associate Fellow.

[‖]Senior Research Engineer, AIAA Member.

[**]Research Director, AIAA Member.

[††]Lecturer, AIAA Member.

[‡‡]Senior Lecturer, AIAA Senior Member.

[§§]Associate Professor.

[¶¶]Graduate Student.

[***]AIAA Senior Member.

[†††]Principal Engineer, Enabling Technology and Research.

[‡‡‡]Technical Fellow, AIAA Associate Fellow.

# I. Introduction

The first two Aeroelastic Prediction Workshops (AePWs), held in 2012 [1] and 2016 [2], respectively, served as focal points for the aeroelastic community to compare their computational aeroelasticity tools and predictive capabilities. During the 2019 International Forum on Aeroelasticity and Structural Dynamics (IFASD2019) conference, the community decided to organize a third workshop (AePW-3), to be held at the AIAA SciTech 2023 conference. The subsequent meetings showed different interests among the aeroelastic community, so workshop activities [3] were split into four working groups: the Large-Deflection Working Group (LDWG), the Flight-Test Working Group (FTWG), the High-Speed Working Group (HSWG), and the High-Angle Working Group (HAWG). The LDWG focuses on analysis of the coupled aeroelastic problems associated with large deflections of a relatively flexible and high aspect ratio wing subjected to low-speed aerodynamics. The FTWG focuses on the body freedom flutter analysis of the NASA experimental flight vehicle X-56A. The HSWG focuses on fluid-structure-interaction analysis at high supersonic to hypersonic speeds, and the HAWG concentrates on the transonic flutter and shock-buffet computations on the Benchmark Supercritical Wing (BSCW) configuration at High-Angles of attack.

Cases selected for the HAWG are listed in Table 1. In this paper, the results for Case #2 are presented. The results for Case #1 are presented in a separate paper [4]. Note that the question mark symbol next to 'Shock buffet' is only indicative of a limited experimental data available for this case. The selection of this shock-buffet case was motivated by several factors. First, analysis shown by Heeg in [1] suggested shock-buffet event at or near conditions selected for the AePW-3. Second, subsequent analysis of the limited experimental data by NASA presented to the community suggested a shock-buffet event. Third, an implied connection between shock-buffet onset and a flutter event at a condition selected for the AePW-3 [1, 5]. And last, an anticipated retest of the BSCW model in the Transonic Dynamics Tunnel (TDT) with plans to include modern optical methods.

The six teams contributing to the shock-buffet predictions are as follows: NASA Langley – Aeroelasticity Branch (NASA), Technion – Israel Institute of Technology (Technion), United States Air Force Academy (USAFA), The University of Newcastle and The University of Sydney (UON), the Indian Institute of Science (IISc), and The Boeing Company (Boeing). Note that the names of each team placed in the parenthesis are used to identify the team in the results section. Some teams have already published their own papers on their computational shock-buffet predictions [6, 7]. Therefore, this paper concentrates on presenting the comparison results and does not venture into a discussion of the shock-buffet physics.

This paper is organized into four sections. Background material on the BSCW configuration and experimental setup with flow conditions are presented first. The pressure coefficient running mean average, Power Spectral Density (PSD) and Strouhal number results at selected pressure sensor locations are presented next. These are generated from the submitted data. The third section presents similar results generated and processed based on using a single solver on the grids provided by select participants. The last section contains a description of each team's numerical processes used to compute shock buffet.

**Table 1    AePW-3 HAWG Workshop Test Cases.**

|  | Case #1 | Case #2 |
|---|---|---|
| Mach | 0.8 | 0.8 |
| AoA | 5° | 5° |
| Dynamic Data Type | Flutter Unsteady | Unforced Unsteady |
| Notes | - Attached / Separated<br>- PAPA exp. data<br>- R-134a | - Shock buffet (?)<br>- OTT exp. data<br>- R-134a |

# II. BSCW Wing Configuration

The Benchmark Supercritical Wing (BSCW) model, shown in Fig. 1, has a simple, rectangular, 16- x 32-inch wing planform with a NASA SC(2)-0414 airfoil. It was first tested in the NASA Langley Transonic Dynamics Tunnel (TDT) [8] in 1991 as part of the Benchmark Models Program test campaign [9]. For this test, the rigid wing was mounted on the TDT Pitch And Plunge Apparatus (PAPA) to obtain the flutter boundary at various Mach numbers and angles
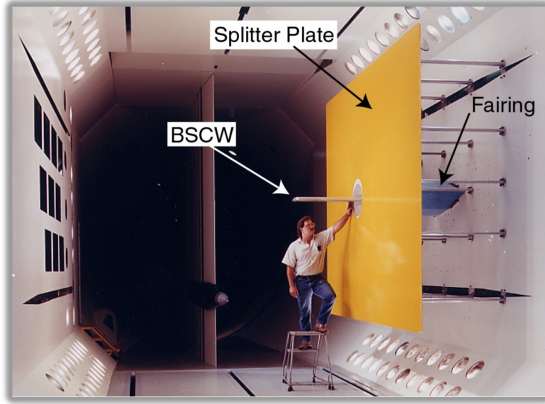
(a) BSCW model mounted on the OTT in TDT [1].
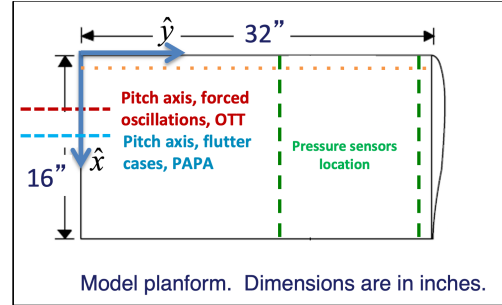
(b) BSCW geometry details.
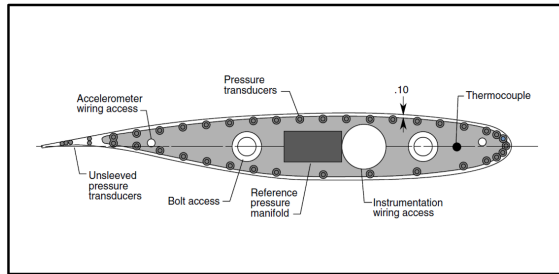
(c) BSCW instrumentation: SC(2)-0414 airfoil.

(d) BSCW reference quantities.

| | | |
|---|---|---|
| Chord | $c_{ref}$ | 16 $in$ |
| Span | $b$ | 32 $in$ |
| Area | $A$ | 512 $in^2$ |
| Moment | $x$ | 4.8 $in$ |
| reference | $y$ | 0 $in$ |
| | $z$ | 0 $in$ |

**Fig. 1    BSCW Model.**

of attack for the two-degree of freedom (pitch and plunge) structure. In 2000, the wing was tested again, this time on an Oscillating Turntable (OTT) [10]. The purpose of the OTT tests was to measure aerodynamic response during sinusoidal (forced) pitch oscillation of the wing. The experimental data indicated that the BSCW exhibited a strong shock and separated flow at a moderate angle of attack in transonic conditions [2]. The OTT test also provided some experimental data for the computational analysis of the shock-buffet environment. Specifically, before each forced oscillation test, the wing was set at a fixed angle of attack, and the unsteady pressure data were collected. The data collected at Mach 0.8 and 5° became a focal point in this study.

For both the OTT and PAPA tests, the model was mounted to a nominally rigid strut and sufficiently offset from the wind-tunnel wall (40 inches) via a large splitter plate in order to (1) place the wing closer to the tunnel centerline and (2) isolate the model from the tunnel wall boundary layer [11]. The wing was designed to be rigid, with the following structural frequencies for the combined wing and OTT mounting system: 24.1 Hz (spanwise first bending mode), 27.0 Hz (in-plane first bending mode), and 79.9 Hz (first torsion mode). When installed on the PAPA mount, the combined system frequencies were 3.33 Hz for the plunge mode and 5.20 Hz for the pitch mode [12].

For instrumentation, the model has pressure ports in chord-wise rows at the 60% and 95% span locations. For the BSCW/PAPA test, both rows were fully populated with unsteady in situ pressure transducers. The quantitative information obtained consists of unsteady data at flutter points and averaged data on a rigidized apparatus at the flutter conditions. For the BSCW/OTT test, only the inboard row at 60% span was populated with transducers. The chord-wise locations of pressure transducers are shown in Fig. 1b, Fig. 2, and are also listed in Table 2. The quantitative information for the OTT test consists of unsteady pressure data and accelerometer data for forced angle-of-attack oscillations and for fixed angle-of-attack conditions. The analysis of the OTT experimental data is described in Reference [13]. In Table 2, the highlighted pressure transducers in red and blue colors are located on upper surface and lower surfaces of the wing, respectively, and were chosen for comparisons between the experimental and the computational data.
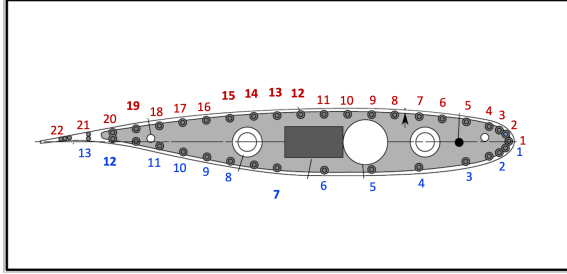
3

**Fig. 2    BSCW Transducer Locations.**

**Table 2    BSCW Transducer Locations.**

| Upper Transducer # | x/c | Lower Transducer # | x/c |
|---|---|---|---|
| 1 | 0 | 1 | 0.012 |
| 2 | 0.009 | 2 | 0.027 |
| 3 | 0.023 | 3 | 0.103 |
| 4 | 0.049 | 4 | 0.203 |
| 5 | 0.099 | 5 | 0.303 |
| 6 | 0.149 | 6 | 0.403 |
| 7 | 0.198 | **7** | **0.503** |
| 8 | 0.249 | 8 | 0.602 |
| 9 | 0.298 | 9 | 0.652 |
| 10 | 0.348 | 10 | 0.702 |
| 11 | 0.398 | 11 | 0.752 |
| **12** | **0.448** | **12** | **0.851** |
| **13** | **0.498** | 13 | 0.901 |
| **14** | **0.542** | | |
| **15** | **0.598** | | |
| 16 | 0.648 | | |
| 17 | 0.749 | | |
| 18 | 0.799 | | |
| **19** | **0.849** | | |
| 20 | 0.899 | | |
| 21 | 0.95 | | |
| 22 | 1 | | |

# III. Shock-Buffet Analysis Results

## A. Experimental Data

The shock-buffet case in the AePW-3 is an extension of a similar case from the AePW-2. The AePW-2 Case 3a assessed the rigid-steady versus rigid-unsteady flow calculations in the presence of a shock-induced separated flow, which dominated the upper and lower aft surface portions of the BSCW model at Mach 0.85, 5° angle of attack. The OTT experimental database consists of several points, as listed in Table 3, where the wing (unforced) was kept at fixed angles of attack at several Mach numbers and dynamic pressures, with unsteady pressures measured at 60% wingspan. One of these experimental points consists of data collected at Mach 0.8 with a dynamic pressure of 170 psf and 5° angle of attack. This experimental point became a focal point for numerical analysis to characterize shock-buffet environment in AePW-3. The experimental conditions are listed in Table 4. The conditions highlighted in red color were chosen for the AePW-3, but conditions at additional dynamic pressures are also provided. Note that Table 3 also lists the motor blade passage frequency. This frequency sometimes may appear in the spectral analysis of the experimental data as will be shown later in this paper.

The experimental data shows the shock motion behavior and location as a function of Mach number and angle of attack. The upper surface mean pressure coefficients are plotted in Fig. 3 across five angles of attack, -1°, 0°, 1°, 3°, and 5°. At Mach 0.7 condition, the shock travels aft with increasing angle of attack. At Mach 0.8, the shock travels aft up to 3° angle of attack then reverses direction at 5° and is located near the mid-chord of the wing. With increasing Mach number and angle of attack, the shock travels farther forward along the wing. An assessment of the local shock induced separation was done by Heeg [13] and showed that at Mach 0.8, and between 3° and 5° angles of attack, the flow field exhibits shock-induced separation onset.

Experimental pressure coefficients were measured at 35 points along the upper and lower surface of the wing at 60% span. These points are shown in Fig. 2. The experimental data was gathered using unsteady pressure sensors with a sampling rate of 1000 Hz. Five seconds of data were collected at each flow conditions.

**Table 3    Unforced BSCW OTT Experimental Flow Conditions.**

| Mach | Dynamic Pressure [psf] | Angle of Attack [°] | Blade Passage Frequency [Hz] |
|------|------------------------|---------------------|------------------------------|
| 0.4  | 100 | 0,1,3,5      | 84  |
| 0.5  | 100 | 0,1,3,5      | 106 |
| 0.5  | 170 | 0,1,3,5      | 104 |
| 0.6  | 100 | 0,1,3,5      | 124 |
| 0.6  | 170 | 0,1,3,5      | 124 |
| 0.7  | 100 | 0,1,3,5      | 149 |
| 0.7  | 170 | 0,1,3,5      | 144 |
| 0.8  | 100 | -1,0,1,3,5   | 166 |
| 0.8  | 170 | -1,0,1,3,5   | 164 |
| 0.8  | 200 | -1,0,1,3,5   | 166 |
| 0.85 | 200 | -1,0,1,3,5   | 179 |
| 0.87 | 100 | -1,1,3,5     | 184 |
| 0.87 | 174 | -1,0,1,3,5   | 184 |

**Table 4    BSCW Flow Conditions: Mach 0.8 with range of dynamic pressure ($q$), chord Reynolds number ($Re_c$), Reynolds number per foot ($Re$), velocity ($V$), speed of sound ($a$), static temperature, ($T_{static}$), density ($\rho$), ratio of specific heat ($\gamma$), viscosity ($\mu$), Prandtl number ($Pr$), total pressure ($H$), and static pressure ($P$).**

| Mach | 0.8 | 0.8 | 0.8 |
|------|-----|-----|-----|
| $q$ [psf] | 100.00 | 168.80 | 200.00 |
| $Re_c$ | 2371336 | 4006103 | 4748658 |
| $Re$ [1/ft] | 1778502 | 3004577 | 3561493 |
| $V$ [ft/s] | 440.21 | 439.88 | 439.70 |
| $a$ [ft/s] | 550.25 | 549.62 | 549.34 |
| $T_{static}$ [°F] | 80.80 | 80.76 | 80.74 |
| $\rho$ [slug/ft$^3$] | 0.001032 | 0.001745 | 0.002069 |
| $\gamma$ | 1.1128 | 1.1133 | 1.1136 |
| $\mu$ [lb-sec/ft$^2$] | 2.555e-07 | 2.554e-07 | 2.554e-07 |
| $Pr$ | 0.68450 | 0.68493 | 0.68513 |
| $H$ [psf] | 399.00 | 673.59 | 798.21 |
| $P$ [psf] | 281.37 | 475.00 | 562.87 |

## B. Numerical Results

Table 5 lists each participating teams' software, mesh type, turbulence model, and time-step size used in each analysis. Figure 4 shows the surface and plane of symmetry mesh used by each team. Participating teams were asked to provide an approximately two-second time vector of coefficient of pressure extracted at the experimental pressure port location 12, 13, 14, 15, 19 on the upper surface and 7, 12 on the lower surface, respectively. These ports are depicted in Fig. 2. In this figure, regions of interest for experimental and numerical comparison are highlighted by bold red and bold blue colors. The running mean of pressure coefficient ($C_p$) time histories is calculated for each numerical solution and compared to experimental data. The results for pressure ports 12, 13, 14, and 19 on the upper surface and 7 and 12 on the lower surface, respectively, are presented in Fig. 5. The running mean of each numerical solution provides information on the pressure magnitude offset with respect to the experimental data. Note that the submitted numerical data sets were examined individually and the initial transients, corresponding to roughly 0.25 seconds of data, were eliminated from the data post-processing. In addition, only 2.5 seconds, out of 5 seconds recorded, of

(a) Mach 0.7, $q$ = 170 psf.

(b) Mach 0.8, $q$ = 170 psf.

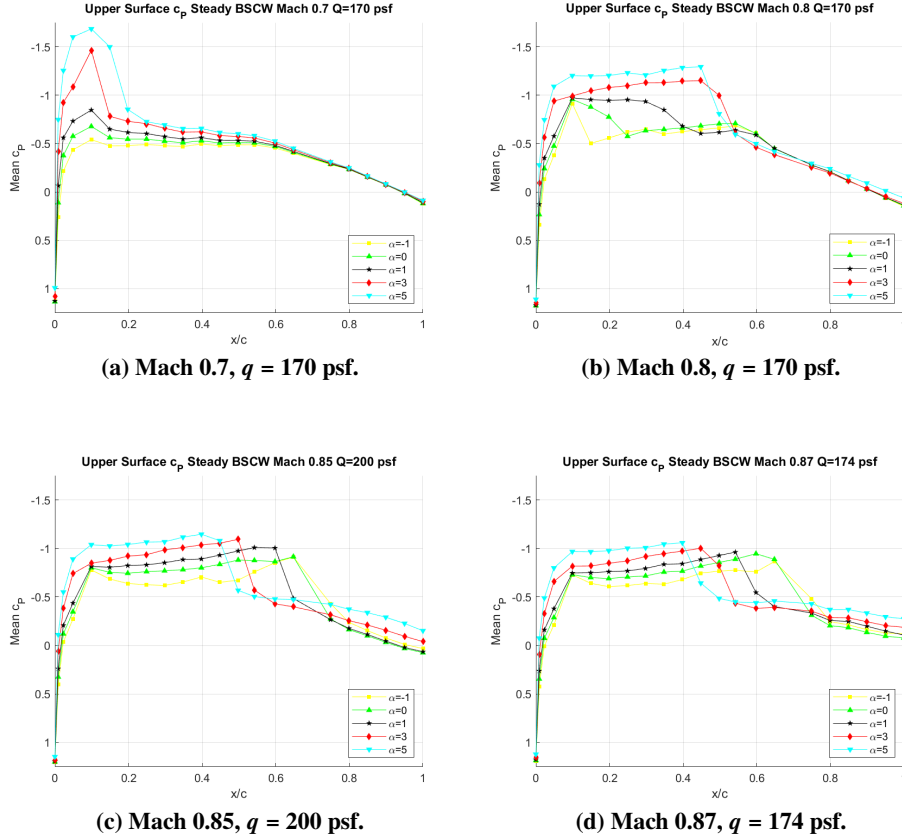(c) Mach 0.85, $q$ = 200 psf.

(d) Mach 0.87, $q$ = 174 psf.

Fig. 3  Fixed wing mean values of pressure coefficients on upper surface across Mach and angles of attack.

the experimental data are plotted. Upper and lower surface pressure coefficient means at each discrete point are also computed (without initial transients) and compared. These are plotted in Fig. 6. Numerically, the mean shock location on the upper wing surface is computed forward of the experimental data. This is also visible in time history plots of pressure coefficient, Fig. 7. In Fig. 7a, for example, the pressure coefficient at the upper port 12 is plotted. Numerical data shows pressure oscillation, while experimental data is quite constant. Experimental data exhibits fluctuations in pressure at pressure-port 13 indicating a shock position aft of what numerical results suggest.

A spectral analysis is applied to all numerical and experimental data by estimating power spectral densities (PSD) of pressure coefficients at points where shocks and separation are expected. The PSDs were applied using the Welch method with 2-3 averaged Hamming windows with 67% overlap on the detrended time histories. Some numerical results had short time signals, which required signal padding to window sizes larger by the next power of two. All time history data are detrended by subtracting full-time sample mean. The PSDs of pressure coefficient for upper surface ports 12, 13, and 19, and lower surface port 12, are shown in Fig. 8. Note that for clarity the results were split into two groups. As pointed out before, some of the experimental data PSD plots show a frequency peak near 160 Hz. This frequency is attributed to the blade-passage frequency as shown in Table 3. Figure 10 shows PSD plots of lift coefficients. Note that due to the high inertial loading environment during OTT testing, no balance was used to measure experimental lift coefficient. Only numerical lift coefficients will be presented. PSD plots were examined individually, and the peak frequencies were extracted. Peak frequency results were grouped around three frequencies of interest and plotted in Fig. 11. The results across the teams show tight frequency groupings for ports 12 and 13. One data set shows an additional peak at Port 12.

Root mean squared (RMS) results of pressure coefficient along the upper and lower surface of the wing are also compared to discrete point experimental results to estimate shock buffet range and relative magnitude. The computed RMS values at 60% wingspan are presented in Fig. 12. While the xy-plot of RMS values show similar distribution across the teams, the contour plots of the RMS over the upper surface of the wing show more differences among teams. The shape of the peak RMS is similar, but the flow activity aft of the peak RMS varies among the teams. The RMS

behavior near the wing root of each result also seems to vary, which may imply some dependence on grid distribution near the symmetry boundary condition, Fig. 13.

**Table 5   Participating teams' software, mesh type, turbulence model, and time-step size.**

| Team | Software | Mesh | Turbulence Model | Time Step (seconds) |
|---|---|---|---|---|
| NASA (section**IV.A**) | FUN3D node-centered | Unstructured Fig. 4a,b,d | SA DDES | $5 \times 10^{-6}$ |
| Technon (section**IV.B**) | EZAir cell-centered | Structured Fig. 4f,g | SA EDW MLC | $1 \times 10^{-4}$ |
| USAFA (section**IV.C**) | Loci/CHEM cell-centered | Unstructured Fig. 4e | SST $k - \omega$ RANS/LES | $1 \times 10^{-5}$ |
| UON (section**IV.D**) | ANSYS® Fluent® 2021R1 cell-centered | Unstructured Fig. 4h | URANS SAS / hybrid RANS-LES | $5 \times 10^{-6}$ |
| IISc (section**IV.E**) | SU2 node-centered | Unstructured Fig. 4a | SA EDW CC | $1 \times 10^{-6}$ |
| Boeing (section**IV.F**) | FELight cell-centered | Unstructured Fig. 4a | SA CC | $3 \times 10^{-5}$ |
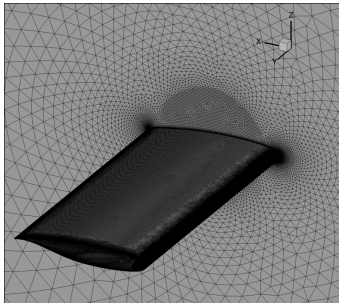


(a) NASA Medium grid 9M (node centered) or 11M (cell centered) nodes.
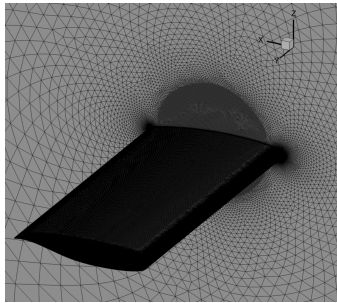
(b) NASA Fine grid, 27M nodes.
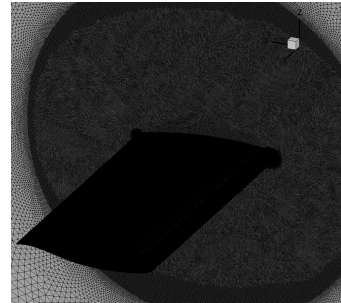
(c) NASA XFine grid, 99M nodes.
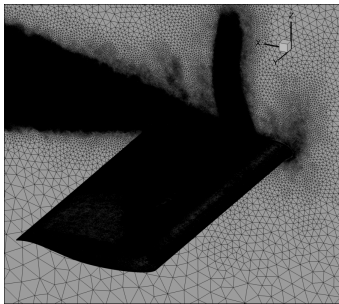
(d) NASA Adapted grid, 60M nodes.
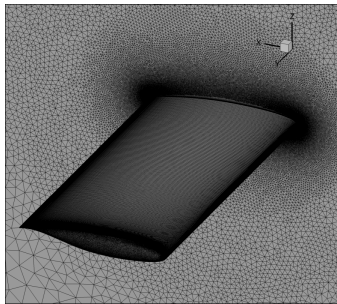
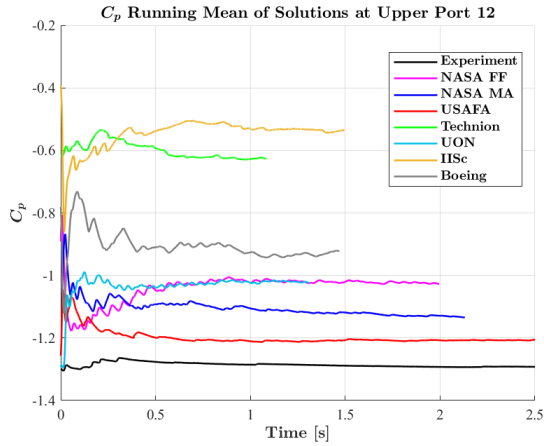(e) USAFA grid, 7M nodes.
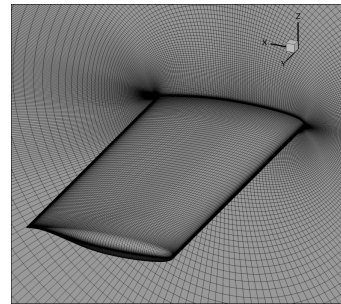
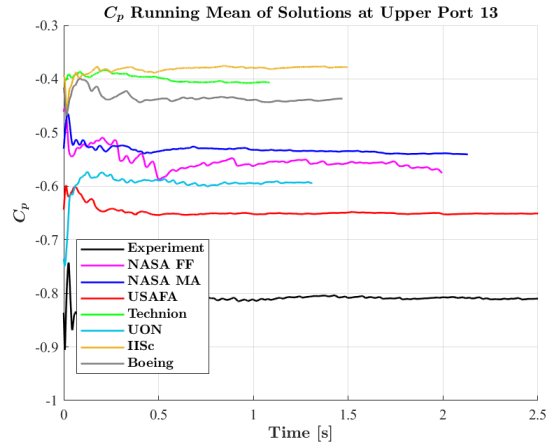(f) Technion Medium grid, 8M nodes.
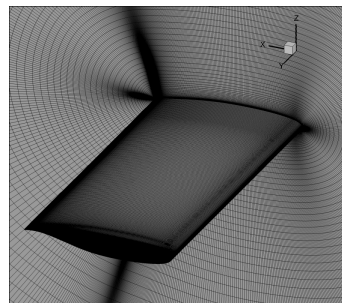
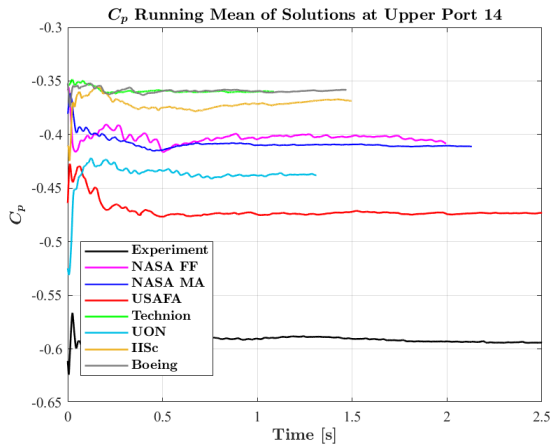(g) Technion Fine grid, 38M nodes.
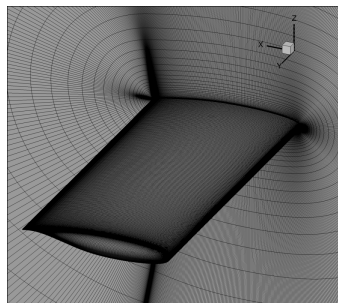
(h) UON grid, 16M nodes.

**Fig. 4   Grids used in buffet computations.**
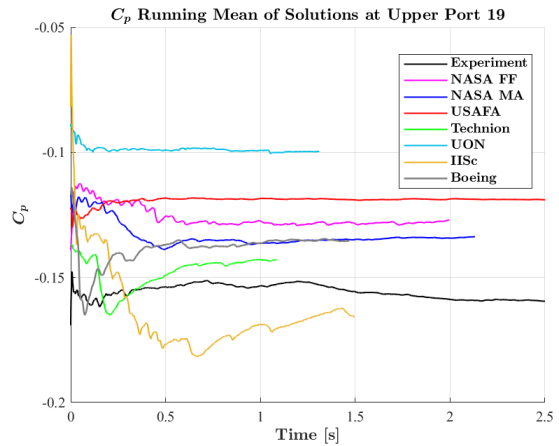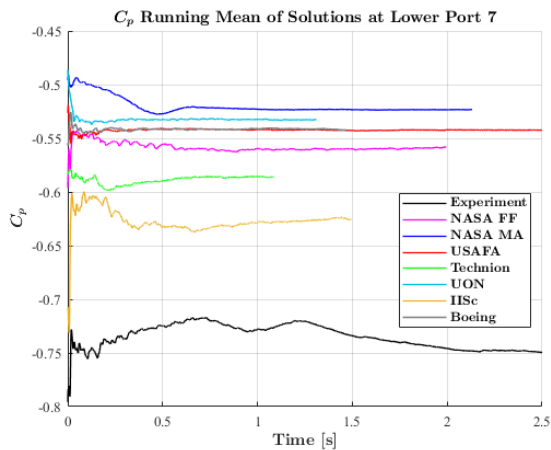
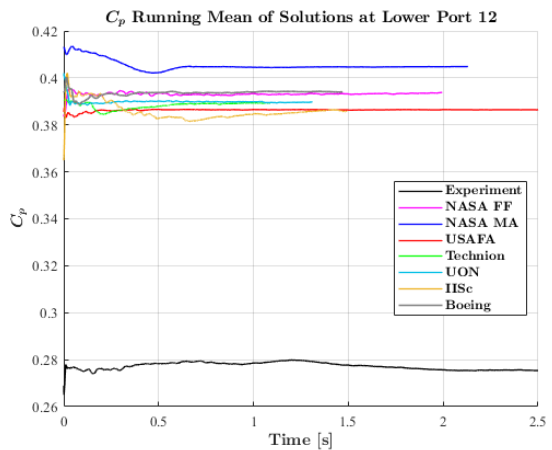**(a) Upper Port 12.**

**(b) Upper Port 13.**

**(c) Upper Port 14.**

**(d) Upper Port 19.**

**(e) Lower Port 7.**

**(f) Lower Port 12.**

**Fig. 5   Running means of pressure coefficients comparing all numerical solutions to experimental results, NASA FF (Fixed Fine Grid), MA (Mesh Adapted) solutions, see section IV.A.**
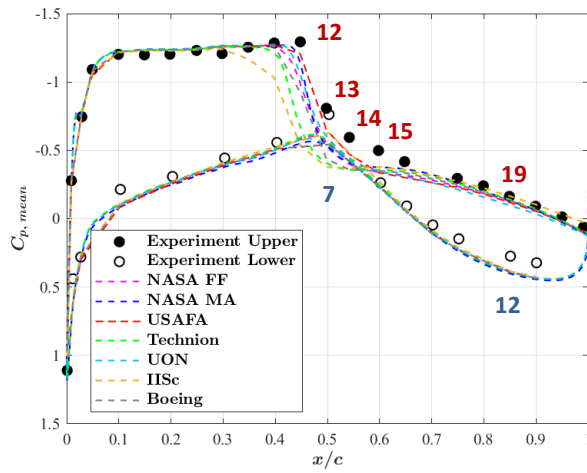
**Fig. 6    Computed mean pressure coefficients compared to experimental results, Mach 0.8, $q$ = 170 psf, angle of attack 5°, upper surface.**
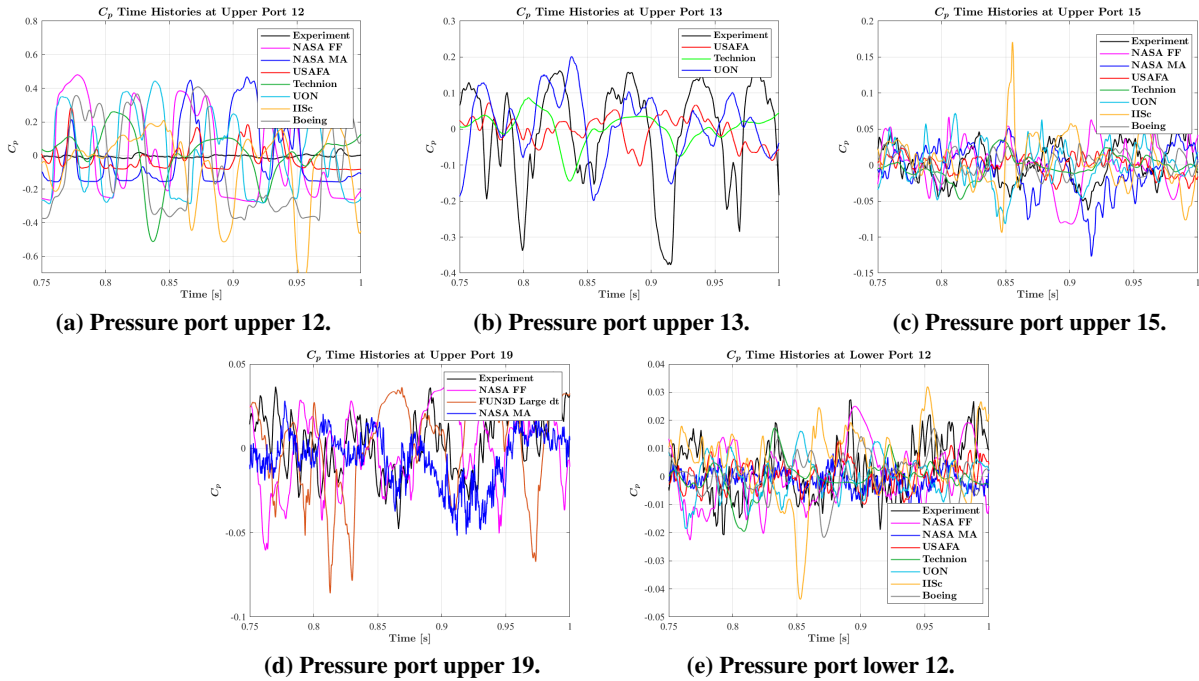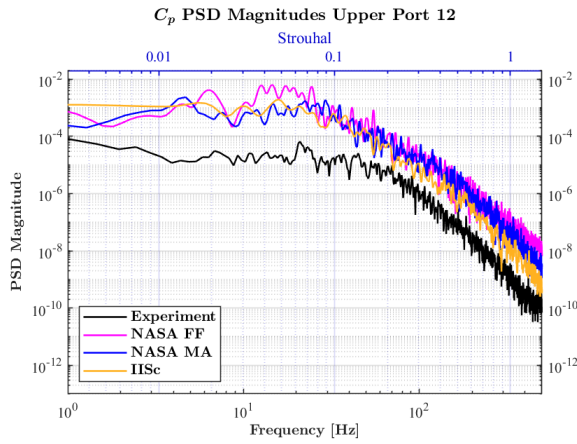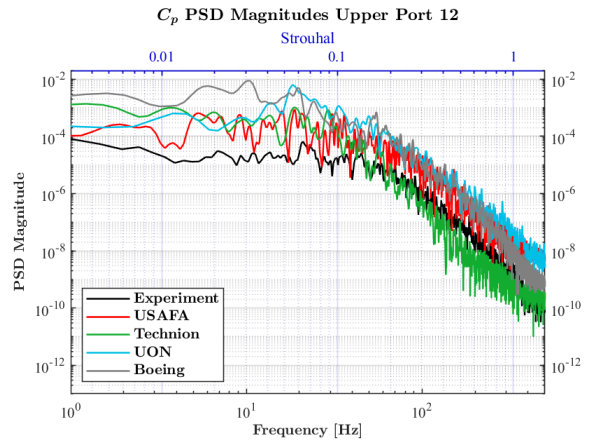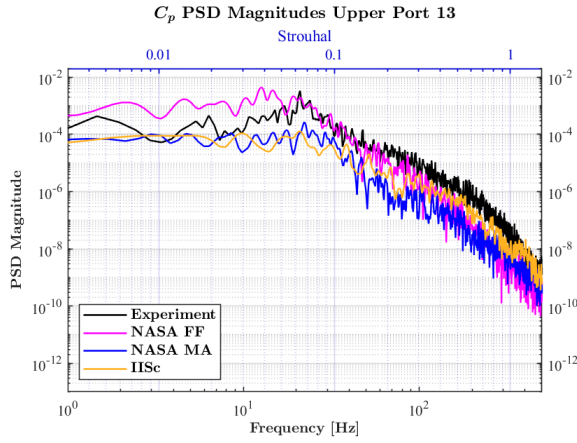


**(a) Pressure port upper 12.**



**(b) Pressure port upper 13.**



**(c) Pressure port upper 15.**



**(d) Pressure port upper 19.**



**(e) Pressure port lower 12.**

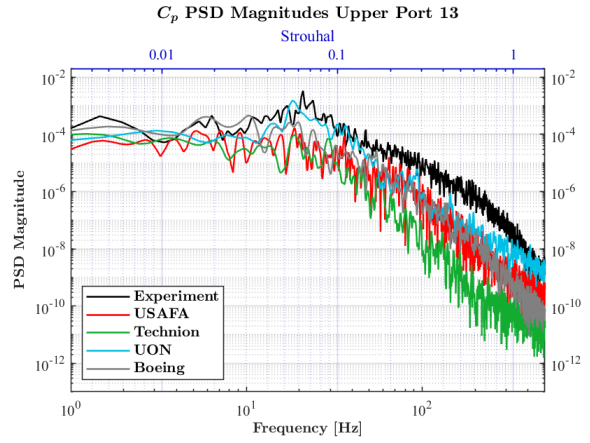**Fig. 7    Time histories of $C_p$, Pressure ports upper 12, 13, 15, 19 and lower 12.**

9

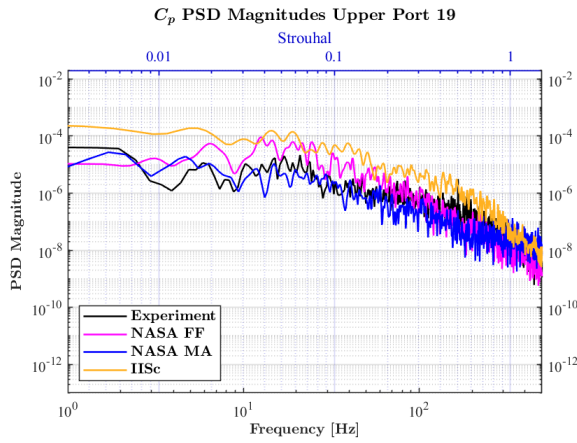(a) **Upper Port 12, Group 1: NASA and IISc.**

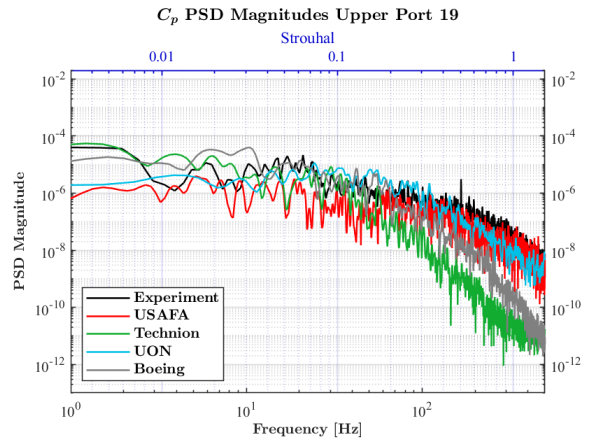(b) **Upper Port 12, Group 2: USAFA, Technion, UON, Boeing.**

(c) **Upper Port 13, Group 1: NASA and IISc.**

(d) **Upper Port 13, Group 2: USAFA, Technion, UON, Boeing.**

(e) **Upper Port 19, Group 1: NASA and IISc.**

(f) **Upper Port 19, Group 2: USAFA, Technion, UON, Boeing.**

**Fig. 8    PSD results of pressure coefficients compared to experimental results, upper ports**
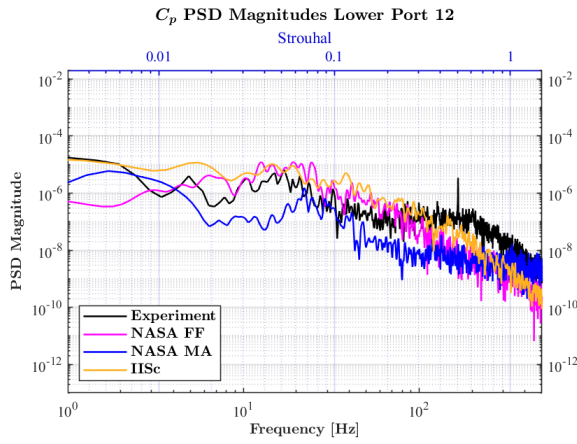
**(a) Lower Port 12, Group 1: NASA and IISc.**
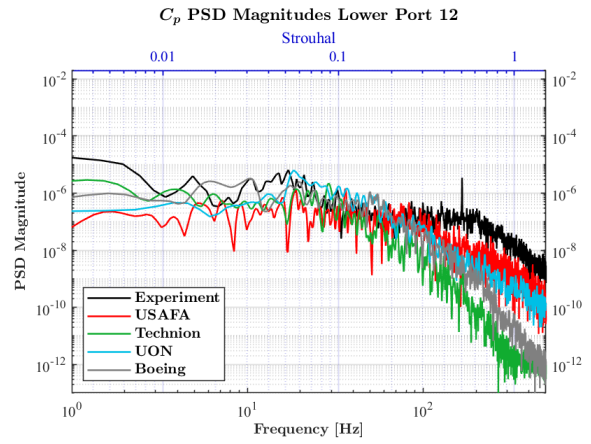
**(b) Lower Port 12, Group 2: USAFA, Technion, UON, Boeing.**

**Fig. 9    PSD results of pressure coefficients compared to experimental results, lower ports.**
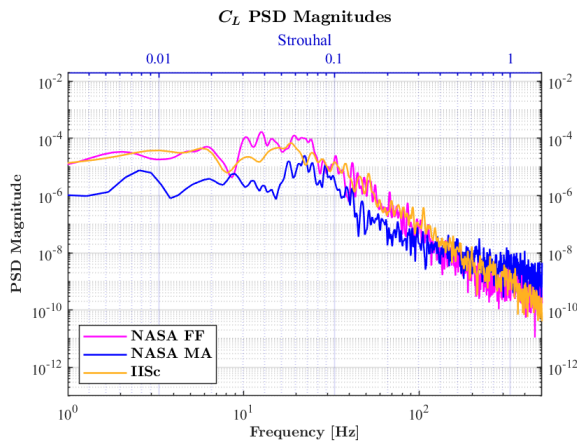


**(a) Lift Coefficient, Group 1: NASA and IISc.**
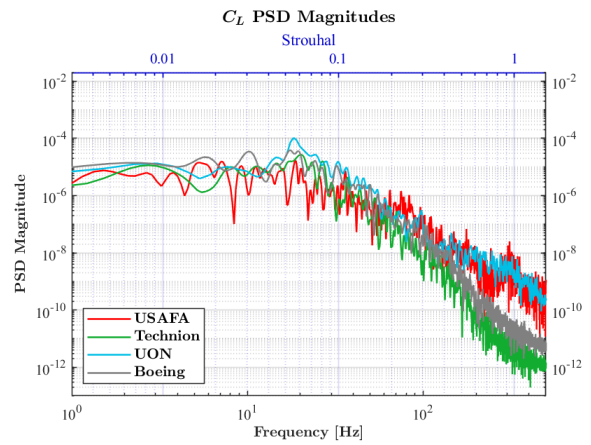
**(b) Lift Coefficient, Group 2: USAFA, Technion, UON, Boeing.**

**Fig. 10    PSD results of lift coefficients.**

11
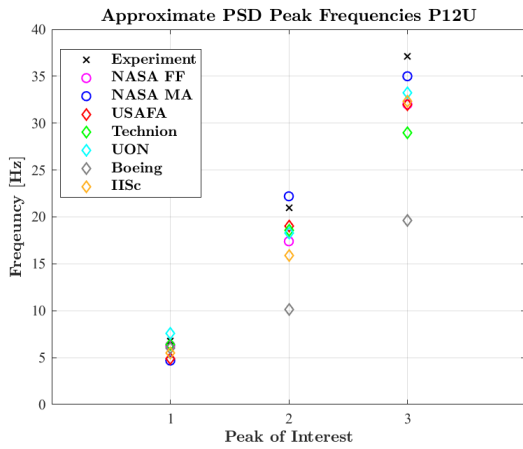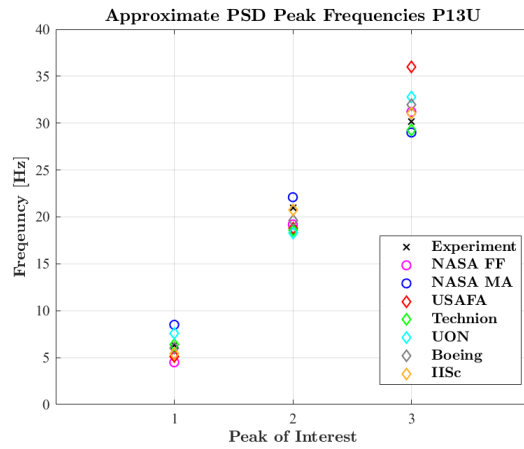
(a) Upper Port 12.
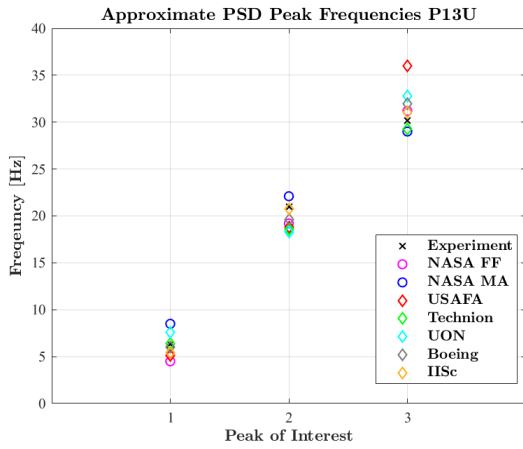
(b) Upper Port 13.

(c) Upper Port 15.
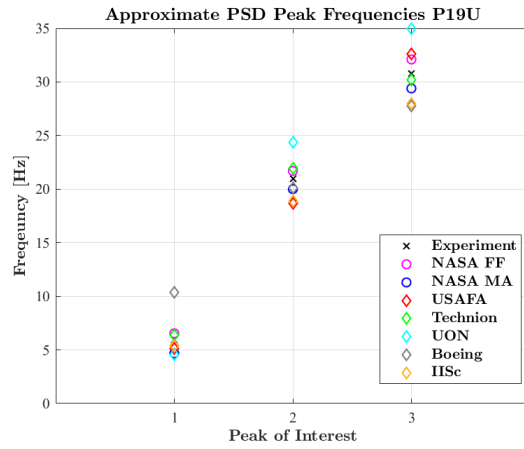
(d) Upper Port 19.
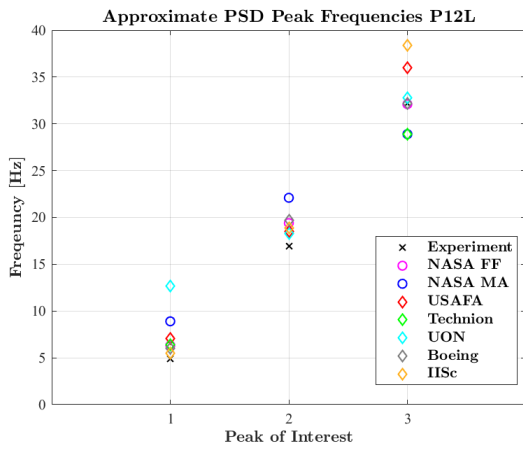
(e) Lower Port 12.
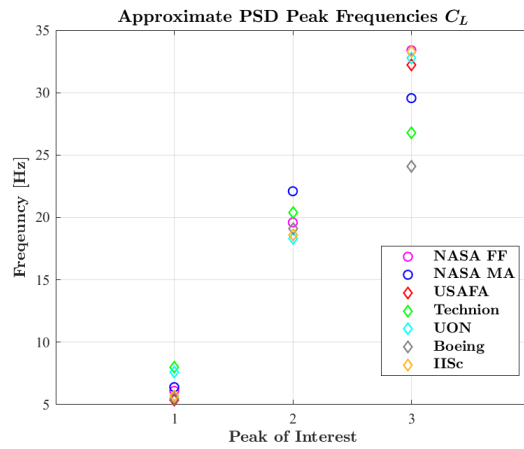
(f) Coefficient of Lift.

Fig. 11    PSD results of pressure coefficients:  peak frequencies.

12

(a) FUN3D-only.

(b) Technion, UON, Boeing.
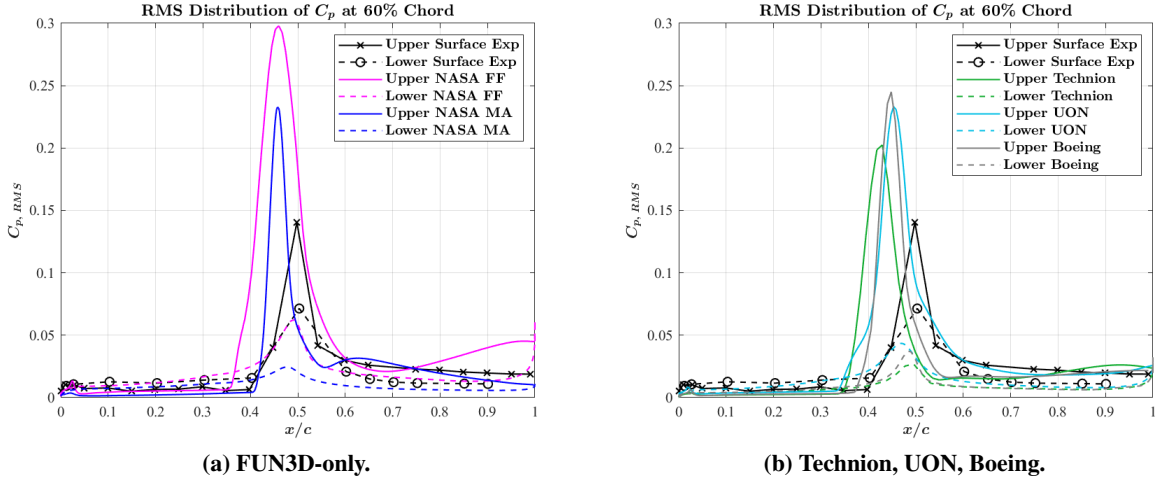
**Fig. 12   Pressure coefficient RMS along the upper and lower surfaces of the BSCW comparing numerical solutions to experimental data.**
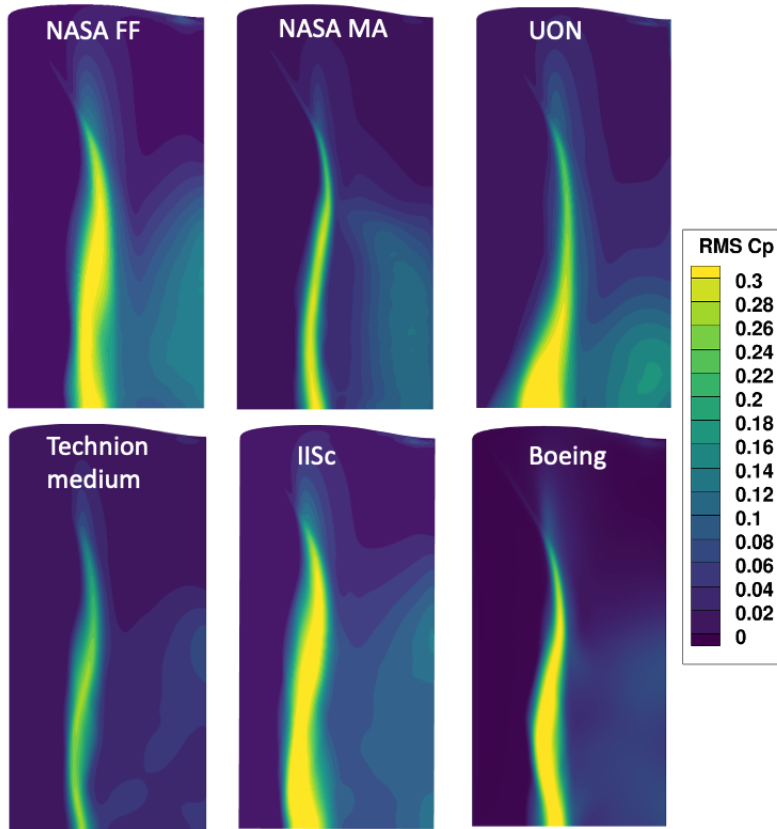


**Fig. 13   Pressure coefficient RMS on the upper surface of the BSCW as computed by each team.**

## C. Same Software, Different Mesh

A numerical exercise was initiated by running a single solver on selected participants grids. Specifically, FUN3D was run with Technion, USAFA, and UON submitted grids. The first step in the process was to check the $y^+$ values. For all grids the $y^+$ values were on the order of one. The same numerical set up was applied to all calculations as described in section **IV.A**. The PSD results are presented, Fig. 14, Fig. 15, Fig. 16, by plotting each team's results at ports 12, 13, and lift coefficients together with FUN3D computed results and experimental data. A cursory look shows similar trends and ranges in computed PSD peaks as in the individual team results. Some differences can be discerned in pressure coefficient RMS values as shown in Fig. 17. More analysis is needed to fully understand this data.



| (a) Port 12, Technion med. mesh. | (b) Port 13, Technion med. mesh. | (c) Lift coefficient, Technion med. mesh. |
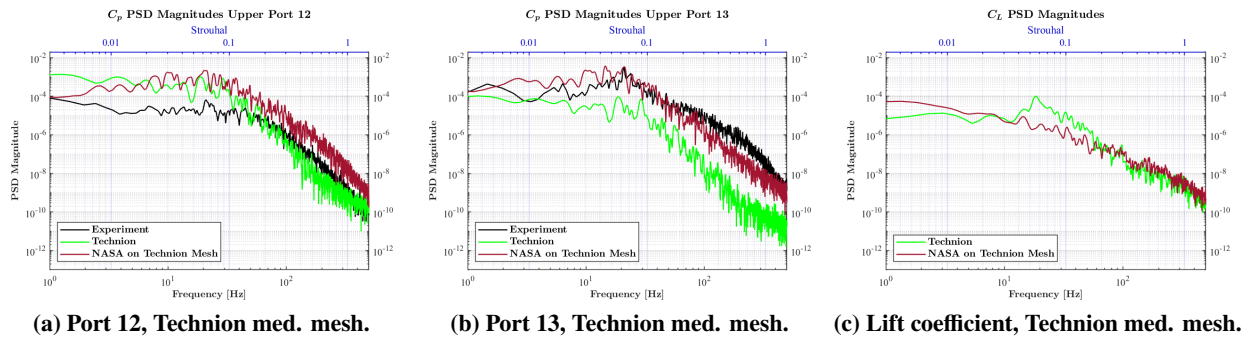
**Fig. 14   PSD results, FUN3D using Technion mesh.**



| (a) Port 12, USAFA mesh. | (b) Port 13, USAFA mesh. | (c) Lift coefficient, USAFA mesh. |

**Fig. 15   PSD results, FUN3D using USAFA mesh.**



| (a) Port 12, UON mesh. | (b) Port 13, UON mesh. | (c) Lift coefficient, UON mesh. |

**Fig. 16   PSD results, FUN3D using UON mesh.**
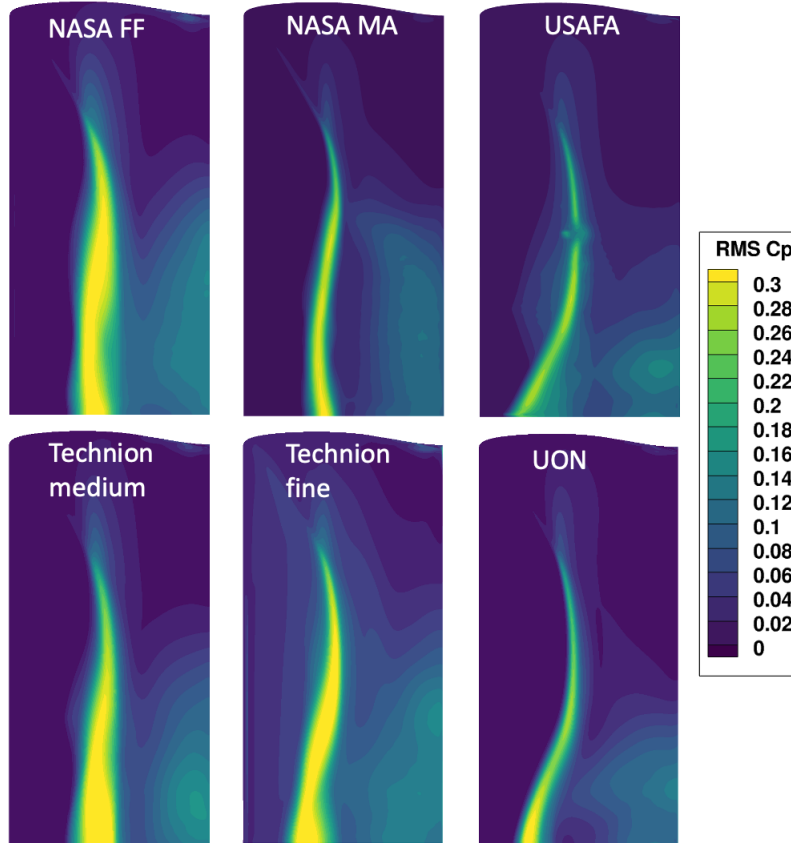
**Fig. 17    Pressure coefficient RMS on the upper surface of the BSCW as computed by NASA/FUN3D on each mesh.**

# IV. Contributing Teams

## A. NASA Langley Research Center - Aeroelasticity Branch

The FUN3D flow solver [14], an unstructured finite-volume node-centered flow solver, is used with the Delayed Detached Eddy Simulation (DDES) method to obtain solutions. The flux limitation was accomplished with the Venkatakrishnan limiter, and inviscid fluxes were computed using the Roe scheme. For unsteady-flow analysis, the FUN3D solver utilizes the dual-time-stepping method. This method involves adding a pseudo-time derivative of the conserved variables to the physical time derivative that appears in the time-dependent Navier-Stokes equations, in much the same way that an artificial time term is often added to the steady Navier-Stokes equations to facilitate an iterative solution to a steady state.

The solutions obtained with the "standard" Spalart-Allmaras (SA) one-equation model with and without different modifications, for example with the Quadratic Constitutive Relationship (QCR) 2000 version, the rotation/curvature correction, and the compressibility correction, did not produce buffeting and requires further attention.

Three grids are considered in the analysis: two fixed grids with wing-only attached to the plane of symmetry and an adapted mesh topology with wing attached to the plane of symmetry. The fixed grids are 27 million and 99 million nodes developed for the first Aeroelastic Prediction Workshop. In the family of grids developed, these grids are considered to be a 'fine' and 'xfine', see Fig. 4. More information on grid development for previous workshop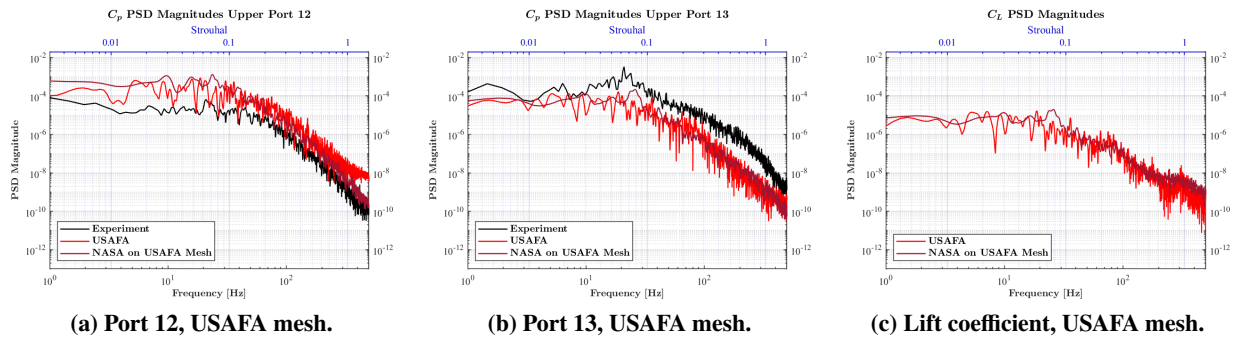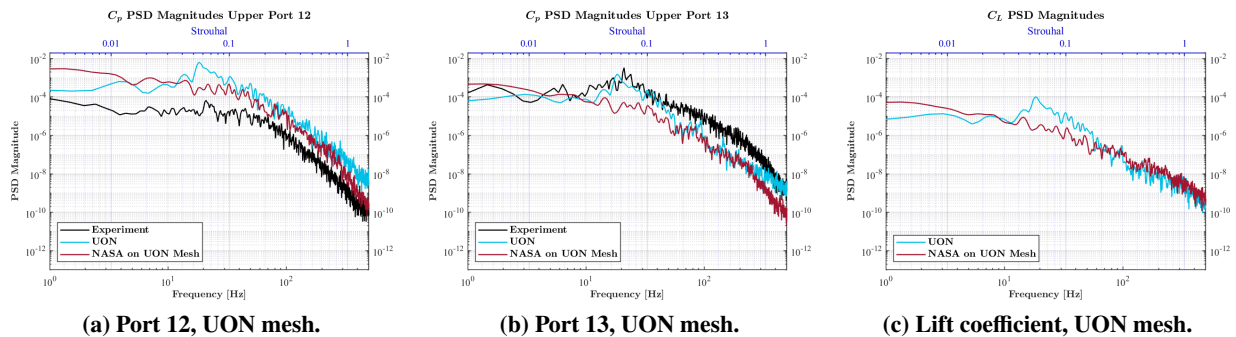s can be found in Ref. [15]. Note that the computations using the xfine grid were not finished in time for this publication and will be published later. Also, the following naming convention is used in presenting our results: 'FF' stands for 'Fixed Fine' grid and 'MA' stands for 'Mesh Adapted', respectively.

For the time-dependent temporal time integration an optimized second-order backward differencing scheme was used [14]. Approximately, five orders of magnitude in residual reduction at subiteration level was achieved with ten subiterations where the residuals asymptotically reached a fixed value.

In the mesh adaptation process, the FUN3D flow solver (unsteady-flow analysis) is linked with a mesh generation software Pointwise®* to adapt the mesh. Here, an isotropic mesh refinement is accomplished by creating point sources at existing mesh nodes, with spacing based on the interpolation error of Mach number. This error is computed by looping through each node in the mesh and comparing the Mach number at that node to a linear least squares interpolation from all nodes in cells containing the node under consideration. For unsteady adaptation, flow states for a series of time steps are examined, and the error from each is accumulated to provide a refinement field that covers all areas containing error. After a new mesh is generated, the existing flow solution is interpolated to the new mesh and the calculation is repeated until mesh convergence is reached. Once a satisfactory mesh refinement is reached, the mesh adaptation process is frozen and the unsteady computations continue to obtain approximately two seconds of data for spectral analysis. The time-step size in the DDES simulation with mesh adaptation is based on the smallest target grid spacing and is set to provide a Courant-Friedrichs-Lewy (CFL) number $\leq 1$. This resulted in time-step size of approximately $\Delta t = 5 \times 10^{-6}$ seconds. Note that this time-step size was used in all fixed-mesh computations as well. A limited temporal resolution study was conducted where the time-step size was increased by one and two orders of magnitude. The cursory examination of these results suggest that the two orders of magnitude increase of the time-step size does not produce enough spectral content in the pressure and the lift coefficient response. These results will be published in the future.

### B. Technion

Flow simulations for the Technion were conducted using the EZAir flow solver [16]. EZAir is a finite volume, structured, multizone, multiblock Euler/Navier–Stokes solver developed by the Israeli CFD Center. Unsteady Reynolds-averaged Navier-Stokes simulations were conducted using the second order in space Harten, Lax, and van-Leer approximated Riemann solver scheme with contact discontinuity treatment (HLLC). The buffet was simulated using the Spalart–Allmaras (SA) model with Edward and Chandra's modification (EDW) [17] and the mixing layer correction (MLC) [18]. The wing mesh is of a C-O type, with $126 \times 361 \times 184$ grid points in the spanwise, chordwise, and perpendicular directions. The first grid cell is located at $1 \cdot 10^{-6}$ m from the wing surface. The resulting normalized wall distance is $y^+ \approx 0.5$ for the simulated flow conditions.

The buffet test case was simulated using the following strategy: Perform a steady-state analysis at a given AoA and Mach values, followed by a time-accurate simulation employing the dual-time stepping method with a time step of $1 \cdot 10^{-4}$ s and a maximum of 50 sub-iterations.

For the buffet test case (Mach 0.8, 5 degrees AoA, and $q_\infty = 170$ psf), unsteadiness was captured only with the SA+EDW+MLC turbulence model (as shown in previous studies), with the mean shock location in a more forward position compared to the experimental data. The details and findings of the BSCW buffet study performed with the EZAir code are presented in Ref. [19].

### C. USAFA

The USAFA utilized Loci/CHEM, a CFD solver developed at the Mississippi State University by Luke et al. [20, 21]. It uses a finite volume scheme with inviscid fluxes calculated using the HLLC inviscid flux scheme by Torro [22]. A low dissipation upwind scheme is also available. The time integration scheme uses a second-order Newton implicit scheme. The solver can be used with moving, deforming and overset meshes.

The solver uses a rule-based programming framework called Loci [23–27]. This Loci-based solver consists of a set of rules, which are scheduled in the Loci framework during execution. Loci takes care of scheduling as well as MPI partitioning and data transfer. This approach simplifies the design of high performance parallel codes. The coding is written in the Loci language, which is converted into C++ code and compiled to an executable.

The simulations are performed as unsteady RANS/LES simulations based on SST $k - \omega$ turbulence model. The time step is $\Delta t = 1 \times 10^{-5}$ seconds, which results in a nondimensional time step of $\Delta t^* \approx 0.005$ and 5 Newton subiterations are used in each time step to converge the solution on the moving mesh.

The computational mesh was generated in Pointwise and contains around 12.5 million cells. It has a prism layer on the surface of the wing and prism and tetrahedral cells in the remainder of the computational volume. The symmetry plane used symmetry boundary conditions, which may potentially affect the results at High-Angles of attack. In the wind tunnel, the symmetry plane is enforced by a splitter plate; the boundary layer on the splitter plate interacts with

---

boundary layer on the wing and, at High-Angles of attack, forms a corner vortex. By using the symmetry boundary condition, we eliminate the boundary layer on the splitter plate and its interaction with the flow around the wing.

## D. The University of Newcastle and The University of Sydney

### 1. Solver Numerics

Simulations from the University of Newcastle and University of Sydney team have been conducted using the commercial, cell-centered finite volume code ANSYS® Fluent® 2021 R1 [28]<sup>†</sup>. The three-dimensional pressure-based implicit solver is used to formulate the coupled set of momentum and pressure-based continuity equations, which are solved segregated from the energy equation. Second-order upwind differencing is used for all convective variables. All diffusive fluxes are treated with a second-order accurate central-difference scheme. Gradients of the convective and diffusive terms are computed at the cell faces through a Green-Gauss reconstruction scheme, with a differentiable gradient limiter employed to mitigate spurious shock oscillations.

### 2. Turbulence modeling approach

Following an earlier sensitivity study [29], Scale-Adaptive Simulation (SAS) [30] has been adopted as the turbulence modeling approach. The SAS method is a so-called advanced URANS model formulation that is able to resolve broadband turbulent fluctuations for globally unstable flows, given appropriate spatial and temporal resolution. The model is developed from the exact turbulent length scale transport equation of Rotta [31], with modifications to include the velocity field second-derivative as a source term. This additional term, not present in conventional RANS formulations, permits adaption of the turbulent length scale to the resolved structures in flow. The SAS formulation offers a further advantage relative to conventional hybrid RANS-LES models in that the turbulent representation reverts to a RANS formulation in the case of coarse spatial and temporal resolution.

For closure of the Navier-Stokes equations, the SAS formulation is coupled with the Stress-Omega Reynolds Stress Model (SORSM), a stress-transport model developed from the $\omega$-equation and the Launder-Reece-Rodi (LRR) model [32]. The SORSM is derived by taking the second-moments of the exact momentum equations, yielding (in a three-dimensional flow) an additional six transport equations for the Reynolds stresses, together with an equation for the dissipation rate. All turbulent transport equations are solved segregated from the coupled set of continuity, momentum and energy equations, with second-order accurate upwind discretization of the turbulent quantities.

### 3. Spatial & temporal discretization

As detailed further in the earlier work of Giannelis et al. [33], three structured, multi-block, hexahedral computational grids have been generated in Pointwise®* for the dedicated transonic buffet analysis of the BSCW under AePW-3. Each grid is constructed through a hybrid hyperbolic/algebraic extrusion of the structured surface grid in the wall-normal direction to a hemispherical farfield approximately 75 chord lengths from the model. Refinement is adopted in the chordwise ($x$) and spanwise ($y$) spacing, as well, as through a reduction in growth rate between the coarse and fine levels. Table 6 summarizes the key metrics for each grid.

**Table 6    University of Newcastle computational grid metrics.**

| Grid | Size ($n_x \times n_y \times n_z$) | First cell height (m) | Growth rate | Cell count (mil) |
|------|------|------|------|------|
| Coarse | $218 \times 133 \times 80$ | $1 \times 10^{-6}$ | 1.22 | 6.3 |
| Medium | $355 \times 200 \times 87$ | $1 \times 10^{-6}$ | 1.20 | 15.6 |
| Fine | $540 \times 300 \times 95$ | $1 \times 10^{-6}$ | 1.18 | 37.0 |

Analysis of the SAS results across the varying levels of spatial resolution indicate the simulations are approaching grid independence at the fine density mesh. To illustrate this point, Fig. 18 compares the computed mean and RMS pressure statistics at each level of grid refinement with the corresponding experimental data points at the 60% span station. The mean pressure distributions computed at each grid level and shown in Fig. 18a are essentially coincident and correlate well with the experiments. At all levels of refinement, the simulations reasonably reproduce the suction surface

---

<sup>†</sup>"Trade names and trademarks are used in this report for identification only. Their usage does not constitute an official endorsement, either expressed or implied, by the National Aeronautics and Space Administration."

pressure roof, trailing edge pressure recovery and the majority of the lower surface distribution. The RMS pressure plots of Fig. 18b indicate that upper surface pressure fluctuations are reasonably well-captured across each level of spatial resolution. While the simulations again display the tendency for an upstream shock displacement relative to the experiments, the range of shock travel and magnitude of pressure fluctuations at 60% span correlates well between the computations and the experiments, particularly for the medium and fine grids. As fairly consistent results are found on both the medium and fine resolution grids using the SAS formulation, the medium grid results are primarily employed to facilitate comparisons under AePW-3.
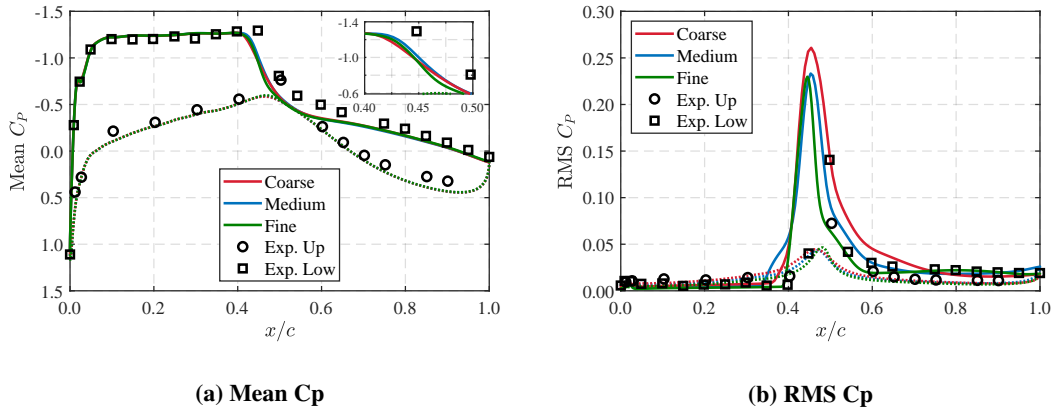


(a) Mean Cp

(b) RMS Cp

**Fig. 18  Comparison between experimental and computed mean and RMS pressure coefficient statistics at varying levels of spatial resolution: (a) - Mean; (b) - RMS.**

Temporal discretization is performed using a second-order backward Euler Dual Time Stepping scheme, with temporal convergence achieved when the relative change in the integral aerodynamic coefficients, averaged over five subiterations, falls below $10^{-7}$. A nominal physical time step of $\Delta t = 5 \times 10^{-6}$ s was also employed in the computations. This is equivalent to a nondimensional time step (with respect to acoustic speed) of $\tau \approx 0.002$, which in the teams' prior experience [34, 35], is somewhat conservative for URANS buffet computations. This is confirmed by a time-step sensitivity study, for which resulting mean and RMS surface pressures at 60% span are shown in Fig. 19 at varying levels of temporal resolution. While a physical time-step of $\Delta t = 5 \times 10^{-5}$ s appears to yield temporally converged results, comparisons are presented for a time-step of $\Delta t = 5 \times 10^{-6}$ s, as longer duration pressure time histories were available for spectral post-processing.
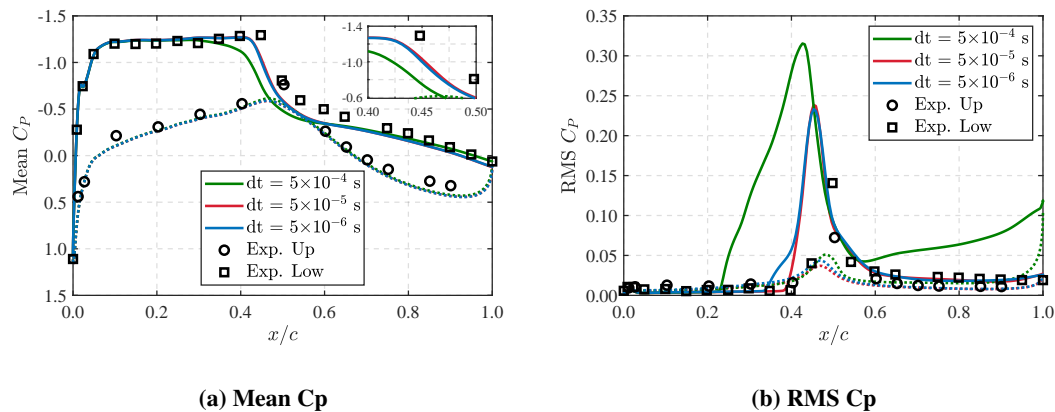


(a) Mean Cp

(b) RMS Cp

**Fig. 19  Comparison between experimental and computed mean and RMS pressure coefficient statistics at varying levels of temporal resolution: (a) - Mean; (b) - RMS.**

## E. Indian Institute of Science

We have simulated the transonic buffet on Benchmark SuperCritical Wing (BSCW) at test case given in Table 1. For that, we have solved unsteady Reynolds-averaged Navier-Stokes (URANS) equations using an open-source suite of codes, namely, the Stanford University Unstructured (SU2) v7.4.0 [36, 37]. Turbulence closure is accomplished using the Spalart-Allmaras eddy viscosity model with Edwards and Chandra modification (EDW) [38], and compressibility correction (CC)[18]. The URANS equations are spatially discretized using a vertex-based finite volume method [36] for an unstructured mesh. The convective flux terms are discretized using the upwind method and evaluated by the flux-difference-splitting scheme of Roe [39] with second-order reconstruction via Monotone Upstream-centered Schemes for Conservation Laws (MUSCL) [40]. The van Albada limiter [41] is used to preserve monotonicity in the solution by limiting the gradients. For the turbulence model, convective terms are differenced using a first-order upwind scheme. The state variables and their gradients for viscus flux terms of RANS and turbulence models are evaluated at vertices using the weighted least-square method, and then they are averaged at control volume faces. The equations are temporally discretized using a second-order implicit Euler backward scheme [36]. The time advancement is achieved by a dual time-stepping strategy [42] in which the equations are converged iteratively to the order of 4 in pseudo-time at every physical time step. Further, the set of linear equations is solved for state variables using the Generalized Minimal Residual (GMRES) linear solver.

There are three grids; coarse, medium, and fine, available from AEPW-2 [43]. The grid topology is shown in Fig. 4a. The grids comprise of three types of elements: tetrahedrons, prisms, and pyramids. Prism elements are very close to the wing's surface, tetrahedrons are in the far-field away from the surface, and pyramids are near to the surface in between prism and tetrahedron elements. The far-field boundary is set at $100c$ ($c$ is chord length) [43]. The details on the three grids, in terms of nodes, $Y^+$, and first cell height, are given in Table 7.

**Table 7    Grid resolution parameters close to surface**

|  | Coarse | Medium | Fine |
|---|---|---|---|
| $Y^+ \approx$ | 1.0 | 2/3 | 4/9 |
| $\Delta y$ (m) | $2.39 \times 10^{-6}$ | $1.6 \times 10^{-6}$ | $1.07 \times 10^{-6}$ |
| Size in million $\approx$ | 3 | 9 | 27 |

Symmetry, no-slip adiabatic wall, and far-field boundary conditions are set on the symmetry plane, BSCW surface, and far-field boundaries, respectively, as shown in Fig. 20.
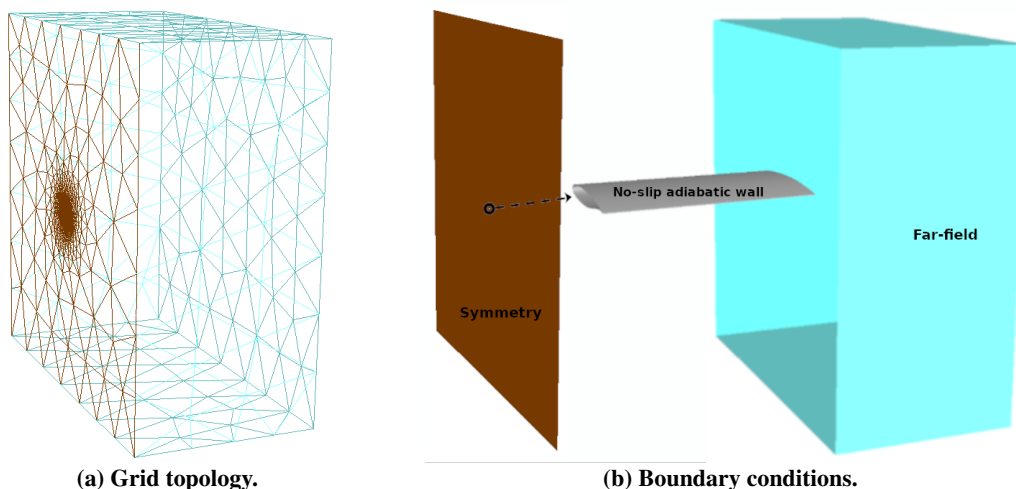


(a) Grid topology.



(b) Boundary conditions.

**Fig. 20    Grid topology and boundary conditions.**

For the grid convergence study, steady simulations on all three grids were performed. Aerodynamic coefficients from these simulations are plotted in Fig. 21a. From these results, medium and fine grids indicate inherent unsteadiness

in the flow; their aerodynamic coefficient values differ, but not by a significant amount. Following that, we have chosen medium grid to have a balance between accuracy and computational cost. For time-accurate simulations, a time-step $1 \times 10^{-6}$ seconds was chosen after a time-step convergence study on the medium grid, as shown in Fig. 21b.



(a) Steady simulation results
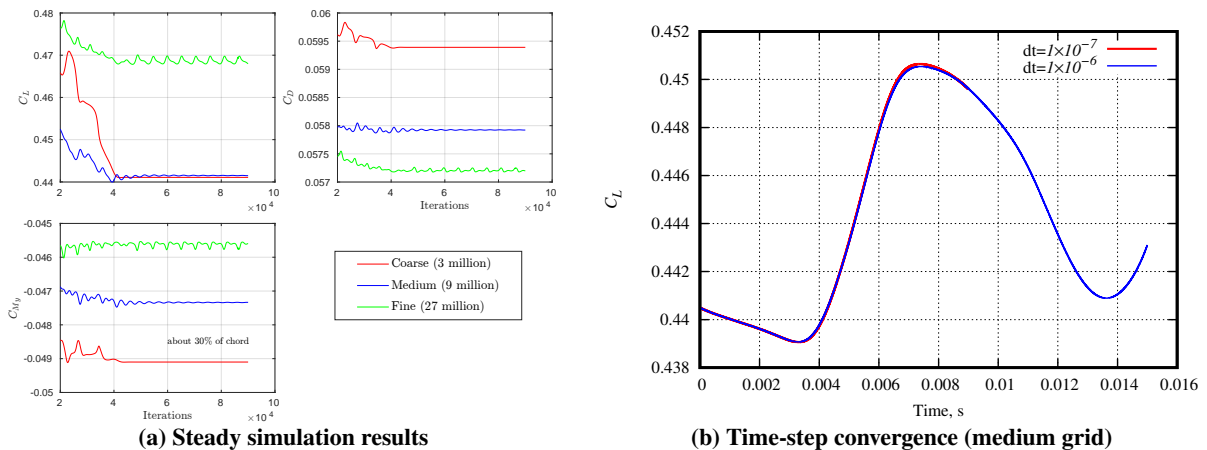
(b) Time-step convergence (medium grid)

**Fig. 21  Grid and time-step convergence studies**

### F. The Boeing Company

In this study, we utilize an in-house Boeing flow solver called FELight. The governing equations consist of the compressible Reynolds-Averaged Navier-Stokes (RANS) equations coupled with the negative version of the one-equation Spalart-Allmaras (SA) turbulence model [44], along with compressibility correction (CC) [45]. For spatial discretization, we employ the Streamwise Upwind Petrov-Galerkin (SUPG) method with linear basis functions. For temporal discretization, we utilize the second-order backward difference formula (BDF2), resulting in second-order accuracy in both space and time. To solve the system of discretized equations, we employ a pseudo-transient continuation (PTC) method [46], in which the physical time term is augmented by a pseudo-time. We discretize the pseudo-transient term using the first-order backward difference formula (BDF1), while the physical term is discretized using BFD2. The resulting implicit system is linearized and solved in a marching manner. To expedite convergence, we compute the pseudo-time for each grid node, resulting in a local time-stepping method. This local stepping is further adjusted by a global CFL number to accelerate convergence. The linearized system is solved using an inexact Newton method, wherein the linear system is solved via an ILU-preconditioned GMRes method [47]. Additionally, we employ a line search process to determine an optimal relaxation factor for the Newton updates, derived from the solution of the linearized system. A CFL number control mechanism is also integrated to regulate the pace of nonlinear advancement. Treating the pseudo-time term as described leads to a dual time-stepping technique [48]. In this technique, the equations for each implicit time step are treated as a modified steady-state problem, which is solved by iteratively progressing through a pseudo-time variable. The described solution strategy closely follows the methods described in Ref. [49]. It is worth noting that the application of the Newton method with ILU-preconditioning and the inclusion of a line search process facilitates achieving deep levels of convergence (down to machine precision) within each time step. In the unsteady solution discussed in this work, the medium grid provided by NASA is used [15], Fig. 4a. Each convection time unit, defined as the ratio of the chord length to the free-stream velocity, is divided into 100 steps. This corresponds to a physical time step size of 3.03e-05 seconds. Subsequently, the nonlinear residual within each step is reduced to 2e-7 before advancing to the next step. On average, this process necessitated 7 sub-iterations, each of which involved solving the linear system with a relative tolerance of 1.0e-3.

## V. Conclusions and Path Forward

The future numerical exercise in shock-buffet computations on BSCW configuration should hinge on additional experimental data. The current available data is quite limited to surface pressure measurements at just one span station. The BSCW wing is scheduled to be retested in Transonic Dynamics Tunnel in the spring of 2025. The plans call for two span stations instrumented with unsteady pressure sensors, heavily instrumented splitter plate to accurately assess

20

the wing-root flow field, and unsteady Pressure Sensitive Paint application. While the participating teams made good progress in shock-buffet analysis, this activity should be re-examined after the new experimental data is available.

The collaborative buffet modeling activities undertaken as part of AePW-3 have made substantial progress in classifying the state-of-the-art in computational aeroelastic capabilities. While results between teams have been fairly consistent with the available experimental data at 60% span, a number of open questions remain. Significant differences in the inboard suction surface fluctuating pressure fields have been noted by participants using various codes and grids. Although this may be attributed to the differing numerics employed, the suitability of a symmetry boundary condition at the splitter plate wall also remains to be confirmed. Additional experimental data with refined spatial resolution along the wing surfaces would aid in addressing this issue. The team further believes, primarily from past experience in similar computations, that the predictive capabilities of URANS modeling approaches at these shock-buffet conditions require further assessment. Reverting to a blind test condition in future AePW iterations, as well as the addition of contemporary experimental data, would be beneficial in attending to this question. Appreciating the limitations of compute resources faced by participants and the requirements of long run-times to acquire sufficient flow results, it may further be advantageous to enforce a consistent frequency resolution in pressure spectra comparisons. In all, the team recommends the continued study of the BSCW as an aeroelastic benchmark. However, the most significant benefits will require additional experimental data and the study of a blind test condition, for which appropriate selection will first require the completion of an experimental campaign.

## Acknowledgments

## References

[1] Heeg, J., Chwalowski, P., Schuster, D. M., Dalenbring, M., Jirasek, A., Taylor, P., Mavriplis, D. J., Boucke, A., Ballmann, J., and Smith, M., "Overview and Lessons Learned from the Aeroelastic Prediction Workshop," IFASD Paper 2013-1A, 2009.

[2] Heeg, J., Wieseman, C. D., and Chwalowski, P., "Data Comparisons and Summary of the Second Aeroelastic Prediction Workshop," AIAA Paper 2016-3121, 2016.

[3] `http://nescacademy.nasa.gov/workshops/AePW3/public/`, 2023.

[4] Chwalowski, P., Stanford, B. K., Jacobson, K. E., Poplingher, L., Raveh, D. E., Jirasek, A., Seidel, J., Pagliuca, G., Berberoff-Naval, J. N., Forster, M., Righi, M., Immordino, G., Ronch, A. D., Lamberson, S. E., Prosser, D., Fadiga, E., Oliani, S., Rondina, F., and Capone, L., "Flutter Prediction Report in Support of the High Angle Working Group at the Third Aeroelastic Prediction Workshop," AIAA Paper 2024, Jan. 2024.

[5] Heeg, J., and Chwalowski, P., "Investigating the Transonic flutter Boundary of the Benchmark Supercritial Wing," AIAA Paper 2017-0191, Jan. 2017.

[6] Poplingher, L., Malik, W., and Raveh, D. E., "Transonic Shock Buffet on the Benchmark Supercritical Wing," AIAA Paper 2022-2314, Jan. 2022.

[7] Giannelis, N. F., and Vio, G. A., "Comparison of URANS and Hybrid RANS/LES buffet response of the Benchmark Supercitical Wing," AIAA Paper 2023-0428, Jan. 2023.

[8] Ivanco, T. G., "Unique Testing Capabilities of the NASA Langley Transonic Dynamics Tunnel, an Exercise in Aeroelastic Scaling," AIAA Paper 2013-2625, Jun. 2013.

[9] Dansberry, B. E., Durham, M. H., Bennett, Rivera, J. A., Silva, W. A., and Wieseaman, C. D., "Experimental Unsteady Pressures at Flutter on the Supercritical Wing Benchmark Model." AIAA Paper 1993-1592-CP, 1993.

[10] Piatak, D. J., and Cleckner, C. S., "A New Forced Oscillation Capability for the Transonic Dynamics Tunnel," AIAA Paper 2002-0171, Jan. 2002.

[11] Schuster, D. M., "Aerodynamic Measurements on a Large Splitter Plate for the NASA Langley Transonic Dynamics Tunnel," NASA TM 2001-210828, Mar. 2001.

[12] Dansberry, B. E., Durham, M. H., Bennett, R. M., Turnock, D. L., Silva, W. A., and Rivera, J. A., "Physical Properties of the Benchmark Models Program Supercritical Wing," NASA Technical Memorandum 4457, 1993.

[13] Heeg, J., and Piatak, D. J., "Experimental data from the Benchmark SuperCritical Wing wind tunnel test on an oscillating turntable," AIAA Paper 2013-1802, Apr. 2013.

[14] "FUN3D 13.7 Manual," URL=https://fun3d.larc.nasa.gov, 2022.

[15] Chwalowski, P., Heeg, J., and Biedron, R. T., "Numerical Investigations of the Benchmark Supercritical Wing in Transonic Flow," AIAA Paper 2017-0190, Jan. 2017.

[16] Kidron, Y., Levy, Y., and Wasserman, M., "The EZAIR CFD Solvers Suite: EZAIR Theoretical and User's Manual - Version 4.59," Tech. Rep. 2020-16, Israeli CFD Center, 2020.

[17] Edwards, J. R., and Chandra, S., "Comparison of Eddy Viscosity-Transport Turbulence Models for Three-Dimensional, Shock-Separated Flowfields," *AIAA Journal*, Vol. 34, 1996, pp. 756–763. doi:10.2514/3.13137.

[18] Spalart, P., "Trends in Turbulence Treatments," *Fluids 2000 Conference and Exhibit*, 2000. doi:10.2514/6.2000-2306, AIAA Paper 2000-2306.

[19] Poplingher, L., and Raveh, D. E., "Shock Buffet and Associated Fluid–Structure Interactions of the Benchmark Supercritical Wing," *AIAA Journal*, Vol. 61, No. 6, 2023, pp. 2381–2399.

[20] Luke, E. D., Tong, X.-L., Wu, J., Tang, L., and Cinnella, P., " CHEM: A Chemically Reacting Flow Solver for Generalized Grids," Tech. rep., AIAA 2003, 2003.

[21] "Chem," URL=http://web.cse.msstate.edu/%7Eluke/chem/index.html, 2019.

[22] Toro, E., Spruce, M., and Speares, M., " Restoration of the contact surface in the HLL-Riemann solver," *Shock Waves*, Vol. 4, 1994, pp. 25–34.

[23] "Loci," URL=http://web.cse.msstate.edu/ĩluke/loci/index.html, 2019.

[24] Luke, E., "Loci: A Deductive Framework for Graph-Based Algorithms," *Third International Symposium on Computing in Object-Oriented Parallel Environments*, edited by S. Matsuoka, R. Oldehoeft, and M. Tholburn, Springer-Verlag, 1999, pp. 142–153.

[25] Luke, E. A., Koomullil, R., and Soni, B. K., "Integrated Multidisciplinary Simulation Environment for Analysis and Testing of RBCC Systems," Final report for nasa grant nas13-98033 delivery order #161, Simulation and Design Center, Mississippi State University, 2 Research Blvd, Starkville, MS 39759, June 2003.

[26] Luke, E. A., Tong, X., Wu, J., Tang, L., and Cinnella, P., "A Step Towards 'Shape-Shifting' Algorithms: Reacting Flow Simulations Using Generalized Grids," *Proceedings of the 39th AIAA Aerospace Sciences Meeting and Exhibit*, AIAA, 2001.

[27] Luke, E., and George, T., "Loci: A Rule-Based Framework for Parallel Multidisciplinary Simyulation Synthesis," *Journal of Functional Programming*, Vol. 14, No. 03, 2005, pp. 477–502.

[28] ANSYS, *Fluent 2021 R1 Theory Guide*, ANSYS Inc, 2021.

[29] Giannelis, N. F., Thornber, B., and Vio, G. A., "Rigid Buffet Response of the Benchmark Supercritical Wing for the Third Aeroelastic Prediction Workshop," *Proceedings of the AIAA SciTech 2022 Forum*, AIAA Paper 2022-0176, 2022.

[30] Menter, F., and Egorov, Y., "The Scale-Adaptive Simulation Method for Unsteady Turbulent Flow Predictions. Part 1: Theory and Model Description," *Flow, turbulence and combustion*, Vol. 85, No. 1, 2010, pp. 113–138.

[31] Rotta, J., "Turbulente strömumgen," BG Teubner Stuttgart, 1972.

[32] Launder, B. E., Reece Jr, G., and Rodi, W., "Progress in the Development of a Reynolds-Stress Turbulence Closure," *Journal of Fluid Mechanics*, Vol. 68, No. 03, 1975, pp. 537–566.

[33] Giannelis, N. F., and Vio, G. A., "Comparison of URANS and Hybrid RANS/LES Buffet Response of the Benchmark Supercritical Wing," *Proceedings of the AIAA SciTech 2023 Forum*, AIAA Paper 2023-0428, 2023.

[34] Giannelis, N. F., Levinski, O., and Vio, G. A., "Influence of Mach Number and Angle of Attack on the Two-dimensional Transonic Buffet Phenomenon," *Aerospace Science and Technology*, Vol. 78, 2018, pp. 89–101.

[35] Giannelis, N. F., and Vio, G. A., "On the effect of control surface deflections on the aeroelastic response of an aerofoil at transonic buffet conditions," *Proceedings of the 28th International Conference on Noise and Vibration Engineering, Leuven, Belgium*, 2018.

[36] Palacios, F., Alonso, J., Duraisamy, K., Colonno, M., Hicken, J., Aranake, A., Campos, A., Copeland, S., Economon, T., Lonkar, A., et al., "Stanford university unstructured (su 2): an open-source integrated computational environment for multi-physics simulation and design," *51st AIAA aerospace sciences meeting including the new horizons forum and aerospace exposition*, 2013, p. 287.

[37] "Stanford University SU2," , 2023. URL `https://su2code.github.io/`.

[38] Edwards, J. R., and Chandra, S., "Comparison of Eddy Viscosity-transport Turbulence Models for Three-dimensional, Shock-separated Flowfields," *AIAA journal*, Vol. 34, No. 4, 1996, pp. 756–763.

[39] Roe, P. L., "Approximate Riemann solvers, parameter vectors, and difference schemes," *Journal of computational physics*, Vol. 43, No. 2, 1981, pp. 357–372.

[40] Van Leer, B., "Towards the ultimate conservative difference scheme. V. A second-order sequel to Godunov's method," *Journal of computational Physics*, Vol. 32, No. 1, 1979, pp. 101–136.

[41] Van Albada, G. D., Van Leer, B., and Roberts Jr, W., "A comparative study of computational methods in cosmic gas dynamics," *Upwind and high-resolution schemes*, Springer, 1997, pp. 95–103.

[42] Jameson, A., and Shankaran, S., "An assessment of dual-time stepping, time spectral and artificial compressibility based numerical algorithms for unsteady flow with applications to flapping wings," *19th AIAA computational fluid dynamics*, 2009, p. 4273.

[43] NASA, "Aeroelastic Prediction Workshop-2," `https://nescacademy.nasa.gov/workshops/AePW2/public/`, 2016.

[44] Allmaras, S. R., Johnson, F. T., and Spalart, P. R., "Modifications and Clarifications for the Implementation of the Spalart-Allmaras Turbulence Model," ICCFD7 Paper ICCFD7-1902, Jul. 2012.

[45] Allmaras, S. R., "Trends in turbulence treatments," AIAA Paper 2000-2306, Jun. 2000.

[46] Kelley, C. T., and Keyes, D. E., "Convergence Analysis of Pseudo-transient Continuation," *SIAM J. Numerical Analysis*, Vol. 35, 1998, pp. 508–523.

[47] Saad, Y., "Iterative Methods for Sparse Linear Systems," *SIAM J. Numerical Analysis*, 2003.

[48] Jameson, A., "Time Dependent Calculations Using Multigrid, with Applications to Unsteady Flows Past Airfoils and Wings," AIAA Paper 1991-1596, Jun. 1991.

[49] Ahrabi, B. R., and Mavriplis, D. J., "An Implicit Block ILU Smoother for Preconditioning of Newton–Krylov Solvers with Application in High-order Stabilized Finite-element Methods," *Computational Methods Applied Mechanics Engineering*, Vol. 358, 2020. 112637.